Journal of Solid State Chemistry 347 (2025) 125325

Contents lists available at ScienceDirect

Journal of Solid State Chemistry

journal homepage: www.elsevier.com/locate/yjssc

Elucidation of atomic and magnetic structures of Al^{3+}-doped Li-ferrite ($LiFe_5O_8$) compounds

S. Inckemann [a], S.-H. Park [a,*], A. Arauzo [b], M. Avdeev [c,d]

[a] Section Crystallography, Dept. Earth and Environmental Sciences, Ludwig-Maximilians-Universität München, Theresienstrasse 41, Munich, 80333, Bavaria, Germany
[b] Instituto de Nanociencia y Materiales de Aragón, Departamento de Física de la Materia Condensada, CSIC-Universidad de Zaragoza, Avenida Reina Mercedes s/n, Zaragoza, 50009, Spain
[c] Australian Centre for Neutron Scattering, ANSTO, New Illawarra Rd, Lucas Heights NSW 2234, Australia
[d] School of Chemistry, The University of Sydney, Sydney, 2006, Australia

ARTICLE INFO

Keywords:
Lithium ferrite-type multiferroics
Polyhedral distortion-induced polarization
Ferrimagnetism
Magnetic structure
Neutron diffraction

ABSTRACT

Chemical stress for structural deformation in $(Li_{0.6}Al_{0.4})(Fe_{0.8}Li_{0.2})_2Fe_3O_8$, denoted as Li60Al40, and $(Li_{0.5}Al_{0.5})(Fe_{0.75}Li_{0.25})_2Fe_3O_8$, denoted as Li50Al50, was achieved by introducing Al^{3+} into α-$LiFe_5O_8$ known as a high-temperature multiferroic. These new solid solution compounds crystallize in the tetragonal space group $\boldsymbol{P}4_32_12$. Their magnetic spin arrangements at 300 K could be determined in the magnetic space group $\boldsymbol{P}4_32_1'2'$ using high-resolution neutron powder diffraction (HRNPD) data. Within the experimental uncertainty in HRNPD, the magnetic moments of Fe^{3+} ions within FeO_6 in the B-sublattice are arranged along the crystallographic $\boldsymbol{c}$ axis and antiparallel to those of FeO_4 in the A-sublattice. In comparison to the Fe-rich Li60Al40, the Fe-poor Li50Al50 shows a stronger dilute effect for the higher Li content at the octahedral site Fe1b. The dilute effect is associated with the lowering of both saturation magnetization and T_C. On the other hand, Li50Al50 shows large electric dipole moments in the strong distorted $(Li, Al)O_6$ and $(Fe, Li)O_6$ polyhedra.

1. Introduction

Spinel ($MgAl_2O_4$)-type compounds including inverse spinels such as magnetite ($Fe^{2+}Fe_2^{3+}O_4$) exhibit diversely correlated physical properties covering multiferroic (MF) couplings, colossal magnetoresistivity, as well as spin liquids and spin glasses, and further quantum critical phenomena [1,2]. To this richness, several structural properties particularly relevant to the present study can be addressed: (1) The coexistence of a diamond-type lattice of AO_4 tetrahedra (A-sublattice) with a pyrochlore-type lattice of triangles of BO_6 octahedra (B-sublattice). The latter is the main basis for geometrically frustrated magnetism in spinel-type compounds [2]; (2) A high chemical flexibility for magnetic and non-magnetic cation types makes it possible for various A- and B-sublattice compositions [1]; (3) The degree of polyhedral distortion along with the order–disorder fashion of A and B cations largely dictates the symmetry lowering of the atomic and magnetic structures with respect to the highest space group (SG) symmetry $\boldsymbol{F}d\bar{3}m$ for spinels [1,3]. The symmetry-breaking at magnetic and/or non-magnetic atom sites plays a relevant role for the magnetoelectricity (ME) in spinels, particularly in the parent structure of the title solid solution compounds, i.e., alpha-lithium ferrite (α-$LiFe_5O_8$, hereafter denoted as LFO) [4–8].

LFO is analog to magnetite with a complicated partial cation-ordering with $2\cdot[Fe^{3+}]$ at the tetragonal A sites and $2\cdot[Li_{0.5}^{+} + Fe_{1.5}^{3+}]$ at the octahedral B sites per 8 oxygens. This complex partial ordering in the B-sublattice results in a symmetry lowering to $\boldsymbol{P}4_332$. Up to date, this acentric, non-polar cubic SG has been considered as the parent symmetry group for its ferrimagnetic spin arrangement along the $\boldsymbol{c}$ axis [5–8]. In this structure model, Li^+ is located at an octahedral special site, *4b* while Fe^{3+} is present at both octahedral *12d* and tetrahedral *8c* sites [9]. In comparison to the magnetite structure (Table 1), the octahedral sites *4b* for Li^+ and *12d* for Fe^{3+} of LFO in $\boldsymbol{P}4_332$ are two independent sites as being split from the octahedral Fe1 site (*16d*) of the magnetite structure in $\boldsymbol{F}d\bar{3}m$.

The point group 432 of LFO disallows spontaneous electric polarization, but does allow the second order ME effect. Indeed, a high ME coupling coefficient (α_{ME}) value of 2 mV/Oe·cm was measured at 120 K in LFO [7]. A α_{ME} value about 0.2 mV/Oe·cm could be measured up to 250 K. In comparison to LFO, the ME coupling values expected for a few

* Corresponding author.
E-mail addresses: sebastian.inckemann@gmx.de (S. Inckemann), sohyun.park@lmu.de (S.-H. Park), aarauzo@unizar.es (A. Arauzo), max@ansto.gov.au (M. Avdeev).

https://doi.org/10.1016/j.jssc.2025.125325
Received 13 November 2024; Received in revised form 7 March 2025; Accepted 13 March 2025
Available online 26 March 2025

Table 1
Atomic parameters of magnetite (an inverse spinel) in $\boldsymbol{F}\bar{4}3m$ [16] and those of the pure lithium ferrite in $\boldsymbol{P}4_332$ [7].

Magnetite (inverse spinel)					
Atomic site	Coordination	Wyckoff position	x	y	z
Fe1	6	16d	0.5	0.5	0.5
Fe2	4	8a	0.125	0.125	0.125
O1		32e	0.2549(1)	0.2549(1)	0.2549(1)
Lithium ferrite					
Atomic site	Coordination	Wyckoff position	x	y	z
Li1	6	4b	0.625	0.625	0.625
Fe1	6	12d	0.125	0.3681(4)	0.8819(4)
Fe2	4	8c	0.9981(4)	0.9981(4)	0.9981(4)
O1		8c	0.3825(15)	0.3825(15)	0.3825(15)
O2		24e	0.1233(10)	0.1318(10)	0.3725(10)

Table 2
Educts in weight% in the synthesis of the title solid solution samples. They are named with the respective Lab code, according to the Li:Al ratio in the starting mixture.

Lab code	Weight%		
	Fe_2O_3	Al_2O_3	Li_2O
Li60Al40	0.8447	0.1079	0.0474
Li50Al50	0.8289	0.1324	0.0388

of magnetite-type MFs, e.g., Co_3O_4 [10] and $CoAl_2O_4$ [11], are higher by a factor of 2.5 [7] but unfortunately below 40 K. Hence, LFO is a rare prototype ME for fabricating composite multiferroics operable at RT [12,13].

The ME effect in α-$LiFe_5O_8$ is associated to the magnetic field (H)-dependent dipole moment of Fe^{3+} (d^5, high-spin) at distorted BO_6 octahedra in the ferrimagnetic spin order below the Curie temperature T_C at ~900 K [14]. The modification of the resulting electric polarization by the spin order of Fe^{3+} [7] is readily succeeded at its polar atomic site C_2, realizing field-dependent spin-orbital coupling [15]. Our aim on this study was to enhance polyhedral distortion by a small-sized and high-charged cation, Al^{3+} in the B-sublattice, as being a driving parameter for magneto-elastically induced electric polarization. This could be succeeded by elucidation of the magnetic structures of two new Al-LFO solid-solution compounds, as described in the followings.

2. Materials and methods

2.1. Sample preparation

The $Li_{1-x}Al_xFe_5O_8$ (x = 0.4 and 0.5) samples were prepared via high-temperature (HT) solid state reaction. The starting oxides were γ-Fe_2O_3 (98%, *Thermo Scientific*), Al_2O_3 (99.5%, *Alfa Aeasar*) and Li_2O (99.5%, *Fox Chemicals*). The optimized ratios for two different solid solution compounds are given with the respective lab code Li60Al40 for $x = 0.4$ and Li50Al50 for $x = 0.5$ in Table 2. For each sample, the starting oxides mixture were homogeneously ground and pressed into several pellets by a hydraulic press with 15 GPa. These pellets within a sintered corundum crucible with a lid were put into an HT furnace (*Nabertherm P 330*) to react at 1300 K for 24 h and then subsequently cooled down to RT at a cooling ramp of 100 K/h. The reacted pellets were ground with an agate mortar and pestle to obtain homogeneous polycrystalline powders for further characterization.

2.2. X-ray powder diffraction (XPD)

The phase identification was performed by Rietveld analysis of XPD data collected on a X-ray powder diffractometer (*XRD3003, GE*) with $MoK_{\alpha 1}$ radiation (Ge(111) monochromator). Each XPD data set was collected on a semiconductor position-sensitive-detector (*Meteor 1D*) in Debye–Scherrer geometry by 2θ scans in a range of 10–135° (2θ). This was repeated 10 times for each sample to add up 10 data sets for a high signal to noise ratio.

2.3. High-resolution neutron powder diffraction (HRNPD)

HRNPD was conducted on the neutron powder diffractometer *ECHIDNA* [17] at the Australian Neutron Source OPAL at *ANSTO*, Sydney. HRNPD data sets were acquired with 1.1 g of Li60Al40 and 0.9 g of Li50Al50 at 300 K. Each sample was packed within a vanadium sample can and located in an Al cryostat. Data collection was performed using a constant wavelength of 1.6215 Å (Ge(335) monochromator) with a step size of 0.05° in a range of 4–164° (2θ).

2.4. Rietveld analysis with XPD and HRNPD data

Phase identification of Li60Al40 and Li50Al50 were made by Rietveld analysis with XPD data using the software package *Jana2020* with the starting model LFO in the cubic space group symmetry (SG) $\boldsymbol{P}4_332$, as given in [9]. There was no distinctively resolved peak splitting in XPD patterns of Li60Al40 and Li50Al50 due to eventual symmetry lowering. However, the difference between the observed and the calculated XPD pattern showed unusual profile residuals, indicating tetragonal reflections superimposed. Hence, further Rietveld analyses with the direct tetragonal subgroups of $\boldsymbol{P}4_332$ were tried (Supplementary Figure A.14). In fact, the tetragonal SG $\boldsymbol{P}4_32_12$ could be selected as the correct SG for both new solid solution compounds by magnetic space group (MSG) determination using neutron diffraction data (see the following sections).

Rietveld refinements were carried out with HRNPD data excluding two data regions: below 10° (2θ) for extremely high background, where there were no Bragg reflections from atomic and magnetic spin arrangements; above 145° (2θ) for intense reflections from the Al cryostat. There are no extra magnetic Bragg reflections over the entire HRNPD patterns of Li60Al40 and Li50Al50, stating ferri-/ferromagnetic orders. Their cubicstructure models in $\boldsymbol{P}4_332$ (Fig. 1a) [9] and the direct tetragonal subgroups, e.g., $\boldsymbol{P}4_32_12$ (Fig. 1b) obtained from Rietveld analyses with XPD data sets were used as the respective starting models to refine atomic structure refinements using HRNPD data. With the propagation vector $k = (0, 0, 0)$, their magnetic subgroups (two cubic and four tetragonal MSGs) were applied to calculate intensities from magnetic contributions in HRNPD patterns. This allows to determine not only the MSG but also ascertains their common tetragonal SG $\boldsymbol{P}4_32_12$. The refined atomic and magnetic structures were visualized using the program *VESTA* [18].

2.5. Evaluation of polyhedral distortion and dipole moments

The distortion of the central atom-ligand distance (Dis_{ligand}) was calculated by comparing the central cation-ligand distances (CV_{dis}) refined with HRNPD data to those of the respective ideal polyhedron (CV_{ideal}). Those CV_{ideal} values were determined by inserting the refined atomic positions of each polyhedron separately into the tool provided by Song et al. [19,20] i.e., $Dis_{ligand} = (\frac{CV_{dis}}{CV_{ideal}} - 1) \cdot 100$. The individual values of Dis_{ligand} of each polyhedron (Supplementary Table A.9) were averaged over the number of vertexes to get the polyhedron distortion degree (Table 7).

The electric dipole moment induced in a distorted polyhedron can be expressed by $\boldsymbol{p}(\boldsymbol{r}_{cm}) = \sum q_i(\boldsymbol{r}_i - \boldsymbol{r}_{cm})$ where $\boldsymbol{p}$ is the electric dipole moment of a distorted polyhedron, $\boldsymbol{r}_{cm}$ is its center position; $\boldsymbol{r}_i$ and q_i are the ligand positions and their charge, respectively. The electric dipole moments of polyhedra in the refined structure models (Table 4) were calculated using the software *Atomsk* [21].

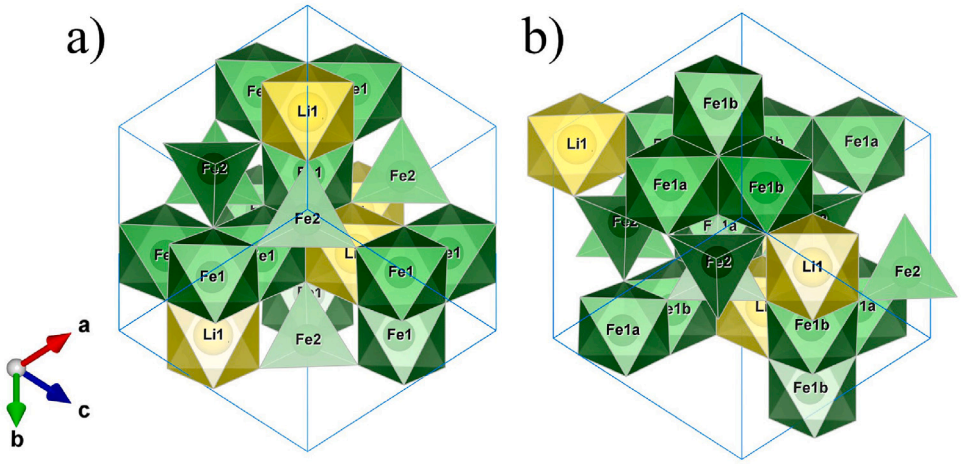

Fig. 1. (a) The lithium ferrite structure model refined in the cubic space group $P4_332$ by Smolentsev et al. [9]. (b) Two Al-LFO solid solution compounds presented in this study crystallize in the tetragonal subgroup $P4_32_12$. Lithium ions (yellow) occupy octahedral sites, and the iron ions (green) occupy both octahedral and tetrahedral sites (see main text).

2.6. Magnetic property measurements

Magnetic property measurements of Li60Al40 and Li50Al50 were carried out in a temperature range of 1.8–390 K on a superconducting quantum interference device (SQUID) magnetometer. Magnetization saturation was determined in a temperature range of 5–305 K with an applied direct current (DC) magnetic field of 10 kOe. For probing field-cooled (FC) DC magnetization data, the samples were cooled down to 1.8 K under magnetic fields, followed by the heating probe up to 390 K. In zero-field cooled (ZFC) measurements, the samples were cooled down to ~12 K and then heated up to 390 K under magnetic fields. The applied magnetic fields were 10 and 1000 Oe for Li60Al40 and 10 and 100 Oe for Li50Al50. The hysteresis loops were obtained from −10 kOe to 10 kOe at 5 and 293 K.

To determine Curie temperatures (T_C), the samples were heated up to 900 K at 1 kOe and subsequently cooled down to 300 K while recording magnetic moments at high temperatures above 300 K on a Quantum Design PPMS VSM magnetometer equipped with an oven option. The T_C points were estimated by linear extrapolation of the data points approaching the paramagnetic magnetic state.

3. Results and discussion

3.1. Phase identification by rietveld analysis with XPD data

Comparison of the XPD data of Li60Al40 and Li50Al50 to that of LFO indicated the pure single phase samples within the experimental resolution. Structural identification of the new Al-bearing solid solution compounds was succeeded by Rietveld analysis. The profiles were refined using a pseudo-Voigt function with axial divergence along with lattice parameters and the detector zero point.

The tetragonal structure models contain atomic sites with lower site symmetries, i.e., site splitting. For instances, as shown in Fig. 2, in the case $P4_32_12$, there are two symmetrically independent octahedral sites for Fe^{3+} at Fe1a (*4a*) and Fe1b (*8b*) which are equivalent to Fe1 (*16d*) for the cubic SG $P4_332$ of LFO. All atomic positions were calculated in consideration of the origin shift. Atomic positions and occupancy (OCC) parameters at all cation sites were refined with soft distance constraints and fixed atomic displacement parameters (ADPs) and the manually determined background to prevent high correlation between parameters. The resulting OCC at Li1(Al1) and Fe1b indicated static disorder with high uncertainty. Nevertheless, XPD data analyses could confirm the new Al-bearing solid solution compounds. The Rietveld refinements with XPD data in $P4_32_12$ are presented graphically in Supplementary Figure A.13.

3.2. SG and MSG determination with HRNPD data

The general process in Rietveld analysis with HRNPD data of Li60Al40 and Li50Al50 is as follows: all profile parameters of the starting models obtained from XPD data analysis were simultaneously refined, as described in the previous section. Subsequently, all atomic positions and site-specific isotropic ADPs were set free to be refined without distance soft constraints. The occupancy parameters at all cation sites were refined, and free variables were fitted for magnetic moments. Note that background points were manually determined and fixed throughout the whole process to prevent their high correlations with OCC, ADPs, and magnetic moments. Otherwise, the convergence could not be reached for high numbers of parameters.

The most difficult step in the structure refinement process was the space group determination for the extremely small tetragonal lattice distortions of the title compounds. Nonetheless, we could ensure the tetragonal SG $P4_32_12$ as the correct symmetry group for the atomic structures of Li60Al40 and Li50Al50 as the best match between the observed HRNPD pattern and the calculated one in the MSG $P4_32_1'2'$. The details in the analysis of HRNPD data of Li60Al40 and Li50Al50 at 300 K are described in the following.

As aforementioned, there are no extra Bragg reflections from the magnetic spin order, explicating the propagation vector k = (0, 0, 0). Accordingly, Rietveld analyses with HRNPD were executed with all possible cubic and tetragonal magnetic subgroups for k = (0, 0, 0), i.e., two cubic MSGs: $P4_3'32'$ and $P4_332$; four tetragonal MSGs: $P4_3'2_1'2$, $P4_32_1'2'$, $P4_3'2_12'$, $P4_32_12$.

After subtracting peak intensities of atomic contribution, there were high residuals of intensities in the small 2θ range below 45° (2θ). This is particularly obvious for the reflection 111 at 19.57° (2θ) whilst refining in the direct magnetic cubic subgroups of the SG $P4_332$, i.e., $P4_3'32'$ (Supplementary Figure A.14a) and $P4_332$ (Supplementary Figure A.14b). Therefore, it was clear that the highest SG symmetry of Li60Al40 and Li50Al50 can be the tetragonal SG $P4_32_12$. Compared to $P4_32_1'2'$ (Supplementary Figure A.14d), the other three tetragonal MSGs led to under- or overestimated magnetic contributions in calculated HRNPD patterns (Supplementary Figure A.14c, e, and f). Hence, our HRNPD data analyses agreed with the ferrimagnetic spin arrangements in the tetragonal MSG $P4_32_1'2'$ for both Al-LFOs. Above all, this MSG clarifies the atomic arrangements in the tetragonal SG $P4_32_12$ and its point group 422. The agreement parameters along with the refined lattice parameters and atomic parameters are given in Tables 3 and 4, respectively. The graphical representations of the respective last cycle of Rietveld refinements with HRNPD data of Li60Al40 and Li50Al50 at 300 K are shown in Fig. 3.

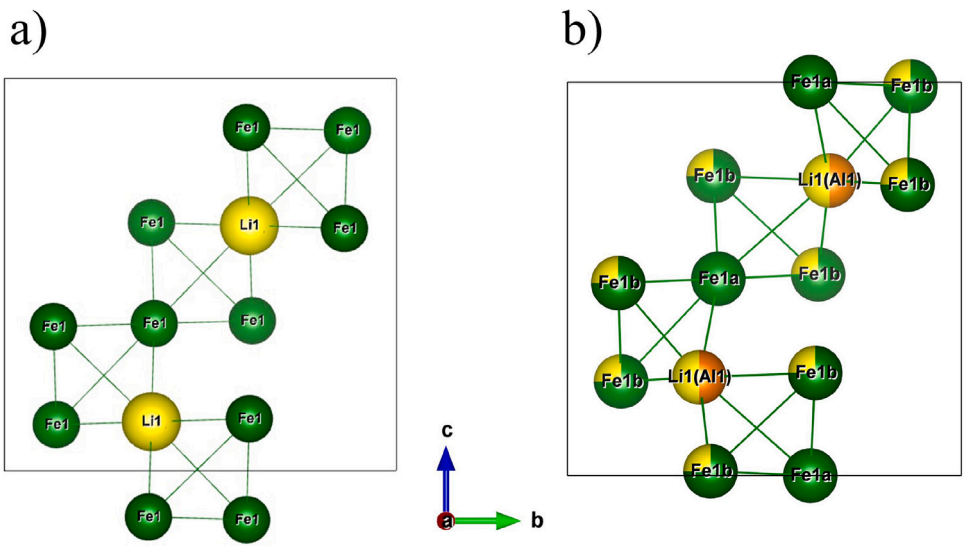

Fig. 2. (a) The so-called B-sublattice of octahedral cations at two unique sites Fe1 and Li1 in the pure lithium ferrite in the cubic space group symmetry $\boldsymbol{P}4_32$, reported by [9]. (b) The B-sublattice of an Al-doped lithium ferrite (Li50Al50) in tetragonal space group $\boldsymbol{P}4_32_12$ with a splitting of Fe sites at Fe1a and Fe1b along with a partial substitution of Al for Li at Li1(Al1). In addition, a part of Fe is replaced by Li at Fe1b.

Table 3
Experimental parameters in neutron powder diffraction data analyses on two different Al-doped lithium ferrite compounds in the magnetic space group $\boldsymbol{P}4_32_1'2'$ at 300 K (wavelength: 1.6215 Å).

Lab code		Li60Al40	Li50Al50
Lattice metric	**a** [Å]	8.2785(3)	8.2677(3)
	c [Å]	8.2630(5)	8.2506(6)
	V [Å^3]	566.29(2)	563.97(3)
R_p [%]		4.33	4.21
R_{wp} [%]		5.96	5.67
GOF		2.56	2.54

$R_p = \frac{\sum_i |y_i(obs)-y_i(calc)|}{\sum_i y_i(obs)} \cdot 100$; $R_{wp} = \sqrt{\frac{\sum_i |w_i(y_i(obs)-y_i(calc))^2|}{\sum_i w_i y_i(obs)^2}} \cdot 100$; $w = \frac{1}{\sigma^2[y_i(obs)]}$;

$R_{exp} = \sqrt{\frac{\sum_i w_i y_i(obs)^2}{n-p}} \cdot 100$; $GOF = \frac{R_{wp}}{R_{exp}}$;

$y_i(obs), y_i(calc)$ = observed and calculated intensity at ith measureing point, respectively;
n = number of observations; p = number of profile points.

We emphasize that the SG symmetry of Al-LFOs is lowered to the tetragonal $\boldsymbol{P}4_32_12$ (SG number: 96) primarily to accommodate non-uniform distribution of Al^{3+}, Li^+, and Fe^{3+}, ensuring the electrostatic charge valence. As previously mentioned, $\boldsymbol{P}4_32_12$ is a maximal subgroup of the cubic SG $\boldsymbol{P}4_32$ (SG number: 212) of LFO. This symmetry lowering splits *12d* Wyckoff sites for Fe^{3+} in the LFO structure into two inequivalent sites *4a* for Fe^{3+} and *8b* for Li^+ statistically disordered with Fe^{3+}. In turn, $\boldsymbol{P}4_32_12$ lowers further into MSG $\boldsymbol{P}4_32_1'2'$ (MSG number: 96.146) for the ferrimagnetic spin orders in Al-LFOs, as described in the next sections.

3.3. Details of the refined atomic and magnetic parameters of Li60Al40 and Li50Al50

3.3.1. Cation distribution

The partial cation-ordering in the B-sublattice dictates the structural and magnetic properties of Li60Al40 and Li50Al50. One of the unexpected results of this study is that the trivalent Al^{3+} resides at a *4a* site available for Li^+ (accordingly this static disorder site is called by Li1(Al1)), rather than at two unique sites available for Fe^{3+}, Fe1a (*4a*) and Fe1b (*8b*) (Table 4, Fig. 4b). As a consequence of the charge excess at Li1(Al1), the necessary electrostatic charge compensation must be brought into the B-sublattice. This could be realized by the static disorder of Li^+ and Fe^{3+} at one of two octahedral sites in the B-sublattice, Fe1b. Interestingly, the other octahedral site, Fe1a (*4a*) and the tetrahedral site Fe2 (*8b*) are fully occupied exclusively by Fe^{3+}. Thus, their OCC values were fixed to be 0.5 and 1, respectively in the last refinement cycle to reduce the number of variables and the correlation with ADPs. It should be mentioned that the OCC parameters 0.503(3) and 0.497(3) at Fe1a in Li60Al40 and Li50Al50, respectively, were obtained at the same fixed ADP value of 0.00745 Å^2. These OCC values indicate full occupation, i.e. OCC = 0.5 of Fe at Fe1a within the experimental uncertainty. However, the presence of a tiny amount of vacancies at Fe1a in Li50Al50 cannot be fully excluded.

Nonetheless, the resulting OCC values could be interpreted unambiguously for the obvious contrast of the coherent neutron scattering length of Li (coh_b(Li) = −1.90 fm) to coh_b(Fe) = 9.45 fm and coh_b(Al) = 3.449 fm. Furthermore, as aforementioned, both octahedral sites Fe1a (*4a*) and Fe1b (*8b*) are independent of each other in $\boldsymbol{P}4_32_12$. Their different atomic site properties, e.g., the preferred occupation of Li^+ at Fe1b, are the clear evidence for the true tetragonal SG symmetry $\boldsymbol{P}4_32_12$ for Li60Al40 and Li50Al50. The refined OCC values at Li1(Al1) and Fe1b in Li60Al40 and Li50Al50 are fairly matched to the respective Li:Al ratio in the starting materials within the experimental uncertainty. From the refined OCC parameters of the cations (Table 4), the structural formulae for these new solid solution compounds could be delivered, as given in Table 5.

3.3.2. Tetragonality

The lattice constants of Li60Al40 and Li50Al50 refined with HRNPD data are compared to those of LFO [7] in Table 6. Al^{3+} has a smaller ionic radius (r = 0.535 Å for octahedral coordination with oxygens) than the respective values of 0.76 and 0.645 Å for Li^+ and Fe^{3+} (high-spin) [22]. The reduction of the metric constants **a** and **c** with increasing the aluminum content accords with the substitution of Al^{3+} in the B-sublattice. The tetragonality of a structure can be expressed simply by the lattice metric difference |**a**–**c**|, resulting in 0.0155(6) Å for Li60Al40 and 0.0171(7) Å for Li50Al50. In this concern, the tetragonality is proportional to the Al-doping. With respect to the cubic lattice constant **a** of LFO, Li50Al50 shows larger lattice contractions in both **a** and **c** than Li60Al40 (Table 6). This is related to large local polyhedral distortions in Li50Al50, as discussed in detail in the next section.

3.3.3. Polyhedral distortion-induced dipole moments

The distortion of cation-ligands were averaged over each polyhedra in Li60Al40, Li50Al50, and LFO, as listed in Table 7. In the parent

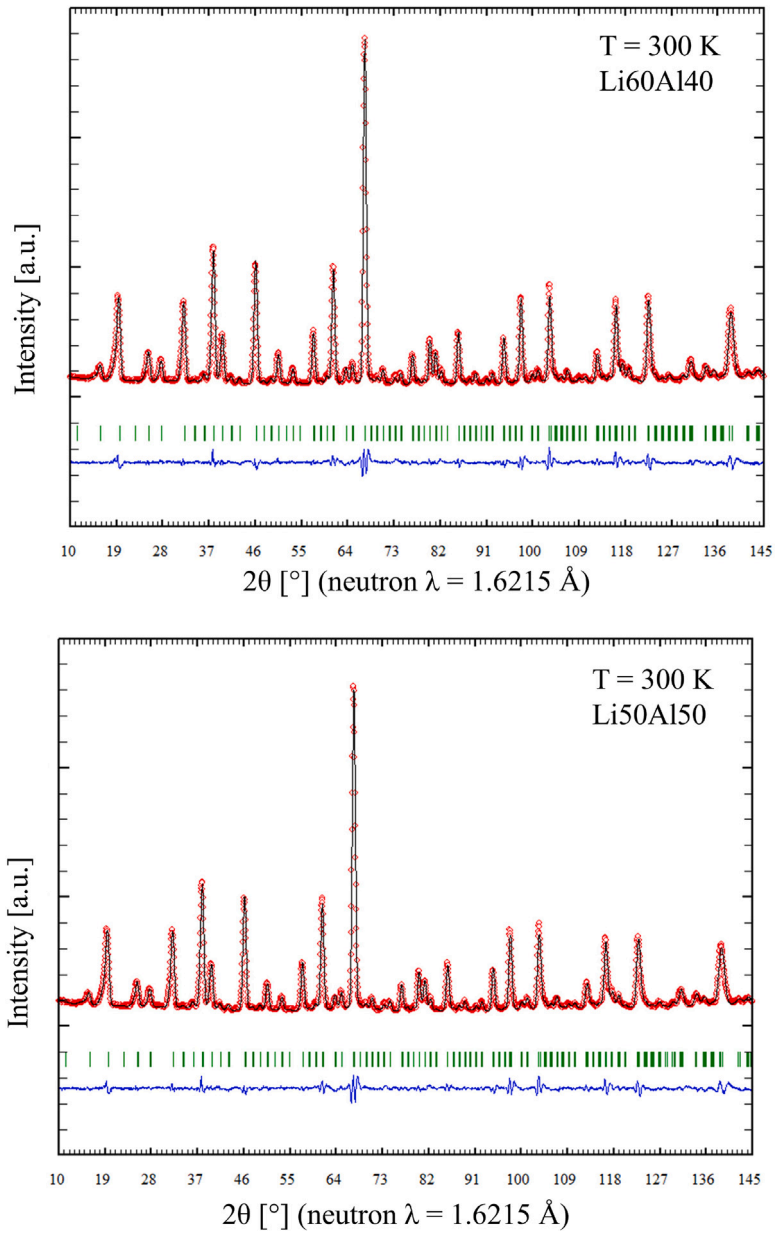

Fig. 3. Graphical presentation of results from Rietveld analysis with HRNPD data of Li60Al40 (top) and Li50Al50 (bottom) at 300 K in the MSG $\boldsymbol{P}4_32_1'2'$. Bragg peak positions from the ferrimagnetic spin order and the atomic orders are superimposed and indicated by green bars. The respective agreement factor for the profile residuals weighted (R_{wp} = 0.0596 for Li60Al40 and 0.0567 for Li50Al50) corresponds to the respective difference profile (blue line) between the observed (red circles) and the calculated profile (black line).

LFO structure, LiO_6 exhibits an almost ideal octahedral geometry with a negligible distortion degree of 0.1(1)%. In contrast, FeO_6 and FeO_4 show a higher distortion degree of 3.7(2) and 1.1(1)%, respectively, inducing the respective electric dipole 0.670(5) and 0.14(1) [eÅ]. The non-zero electric polarizations at the polar atomic symmetries C_2 and C_3 [15] for the magnetic Fe^{3+} within FeO_4 and FeO_6 are regarded as being essential to the spin-orbital coupling in LFO [7].

This relevant polyhedral distortion effect could be enhanced by the partial cation-ordering in the Al-doped LFO-compounds as the distortion degree of $(Li, Al)O_6$ increases dramatically up to 10.5% in Li60Al40 and 12.8% Li50Al50, i.e., proportional to the Al content of 40 and 50 at.% at Li1(Al1) in Li60Al40 and Li50Al50, respectively. In the case of $(Fe, Li)O_6$ compared to $(Li, Al)O_6$, a relatively smaller difference in the ionic radii between Fe^{3+} and Li^+ with low amounts of Li at Fe1b (20 at.% in Li60Al40 and 25 at.% in Li50Al50) give rise to smaller distortion of $(Fe, Li)O_6$ than $(Li, Al)O_6$, i.e., 3.4% in Li60Al40 and 3.9% in Li50Al50. In addition, the distortion of FeO_4 in Li50Al50 (3.3%) is larger than that in Li60Al40 (2.3%). As a result, the overall electric dipole modulus induced by polyhedral distortions in Li50Al50 is larger than that in Li60Al40 (Fig. 5, Table 7).

In summary, there is a clear correlation between the polyhedral distortion and the Al:Li ratio (thus the Li:Fe ratio at Fe1b) in the LFO topology. This means that the chemical stress with Al^{3+} makes it easy to tune the electric polarization at polar atomic sites for magnetic Fe^{+3} in the LFO-type MFs. The consequent Fe-dilute effects on the magnetization in both Al-LFOs are presented in the next sections.

3.3.4. *New ferrimagnetic structures of Al-doped LFO-type compounds*

The tetragonal magnetic structure model is further confirmed by the magnetic moments at the iron sites. In the case of the cubic MSGs (Supplementary Table A.10), either the octahedral iron site (Fe1) in $\boldsymbol{P}4_332$ (Supplementary Figure A.15a) or the tetrahedral site Fe2 in $\boldsymbol{P}4_3'32'$ (Supplementary Figure A.15b) would have a total magnetic moment close to zero. The spin arrangements in space diagonal directions

Table 4
Atomic parameters refined with HRNPD data of Li60Al40 and Li50Al50 at 300 K. Isotropic ADPs (Uiso) were refined with the constraint: Uiso(Li1(Al1)) = Uiso(Fe1a) = Uiso(Fe1b) = Uiso(Fe2). Uiso for all four oxygen sites were group-specific refined, as well.

Lab code	Site	Type	Coordinates			Occupancy	Uiso [Å^2]	Wyckoff site
			x	y	z			
Li60Al40	Li1(Al1)	Li	0.157(19)	0.157(19)	0	0.306(7)	0.0062(3)	*4a*
		Al				0.193(7)	0.0062(3)	
	Fe1a	Fe	0.617(1)	0.617(1)	0	0.5	0.0062(3)	*4a*
	Fe1b	Fe	0.872(1)	0.361(1)	0.007(1)	0.805(4)	0.0062(3)	*8b*
		Li				0.195(4)	0.0062(3)	
	Fe2	Fe	0.750(1)	0.996(1)	0.122(1)	1	0.0062(3)	*8b*
	O1	O	0.149(1)	0.381(2)	0.508(2)	1	0.0060(3)	*8b*
	O2a	O	0.871(2)	0.130(2)	0.512(1)	1	0.0060(3)	*8b*
	O2b	O	0.125(2)	0.113(2)	0.252(1)	1	0.0060(3)	*8b*
	O2c	O	0.870(2)	0.380(2)	0.240(2)	1	0.0060(3)	*8b*
Li50Al50	Li1(Al1)	Li	0.165(6)	0.165(6)	0	0.24(2)	0.0054(3)	*4a*
		Al				0.26(2)	0.0054(3)	
	Fe1a	Fe	0.617(1)	0.617(1)	0	0.5	0.0054(3)	*4a*
	Fe1b	Fe	0.871(1)	0.363(1)	0.011(1)	0.75(1)	0.0054(3)	*8b*
		Li				0.25(1)	0.0054(3)	
	Fe2	Fe	0.752(1)	0.992(1)	0.123(1)	1	0.0054(3)	*8b*
	O1	O	0.150(1)	0.383(2)	0.508(2)	1	0.0062(4)	*8b*
	O2a	O	0.872(2)	0.128(2)	0.511(1)	1	0.0062(4)	*8b*
	O2b	O	0.126(2)	0.115(2)	0.252(1)	1	0.0062(4)	*8b*
	O2c	O	0.869(2)	0.377(2)	0.236(1)	1	0.0062(4)	*8b*

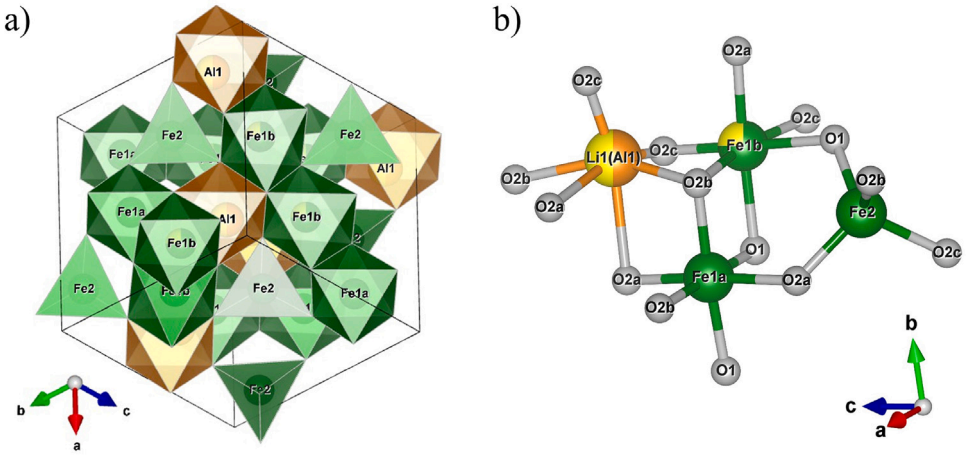

Fig. 4. (a) A polyhedral structure model of $(Li_{0.5}Al_{0.5})(Fe_{0.75}Li_{0.25})_2Fe_3O_8$ (denoted as Li50Al50) in the tetragonal space group symmetry $\boldsymbol{P}4_32_12$. (b) The connection of four independent structure-building polyhedra in Li50Al50 with colored indication of the partial static disorder, i.e., the occupation portion of Li, Al and Fe are in yellow, orange and green, respectively.

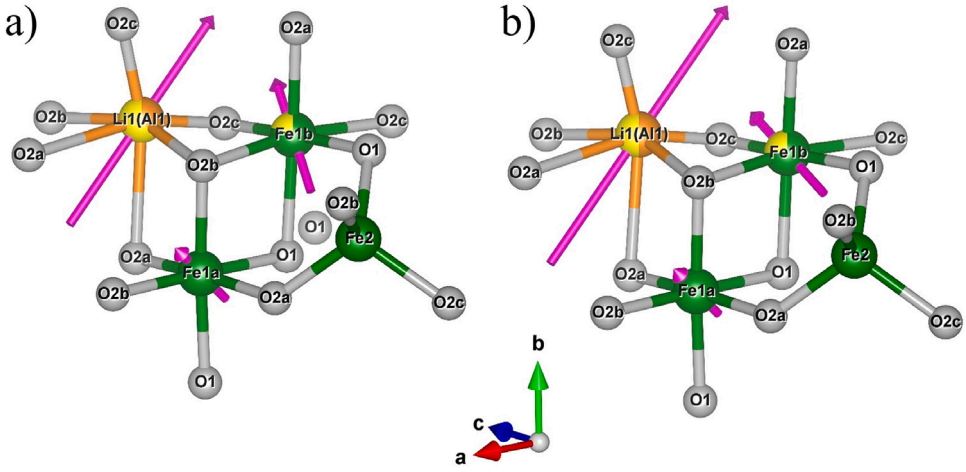

Fig. 5. Polyhedral distortion-induced electric dipole moments (pink) in Li60Al40 (a) and Li50Al50 (b). These structures comprise strongly distorted polyhedra, resulting in relatively large electric dipole moments, particularly $(Li, Al)O_6$ and $(Fe, Li)O_6$ in the B-sublattice. This elastic effect is more dominant in Li50Al50 (b) than Li60Al40 (a) and LFO (see Table 7).

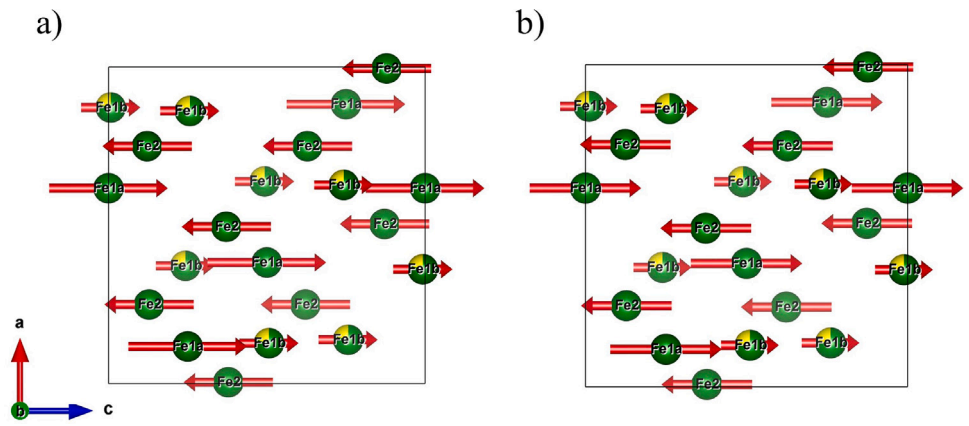

Fig. 6. The ferrimagnetic arrangement of Fe^{3+} in Li60Al40 (a) and that of Li50Al50 (b). The ferrimagnetic unit cell coincides with the atomic unit cell.

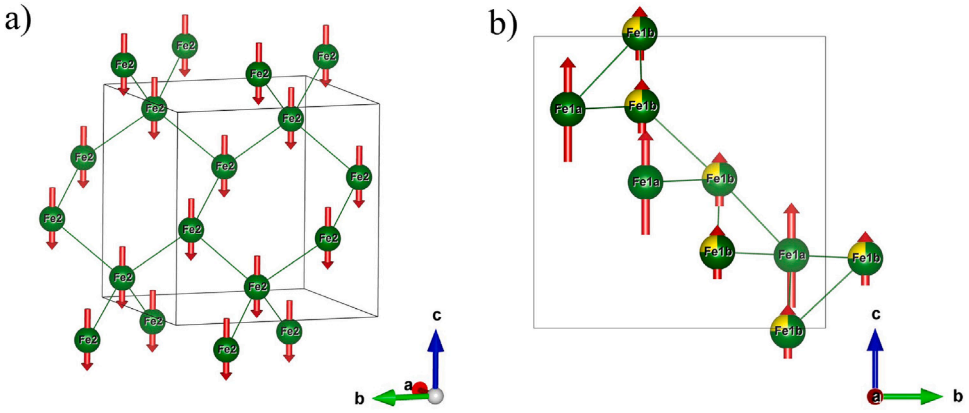

Fig. 7. The A-sublattice of Fe^{3+} at Fe2 in Li50Al50 (a) exhibits collinear spin alignments with respect to [00$\bar{1}$] at 300 K, i.e., antiparallel to the magnetic spin alignment in the B-sublattice (b). The green lines indicate the nearest Fe–Fe distances within 4.0 Å.

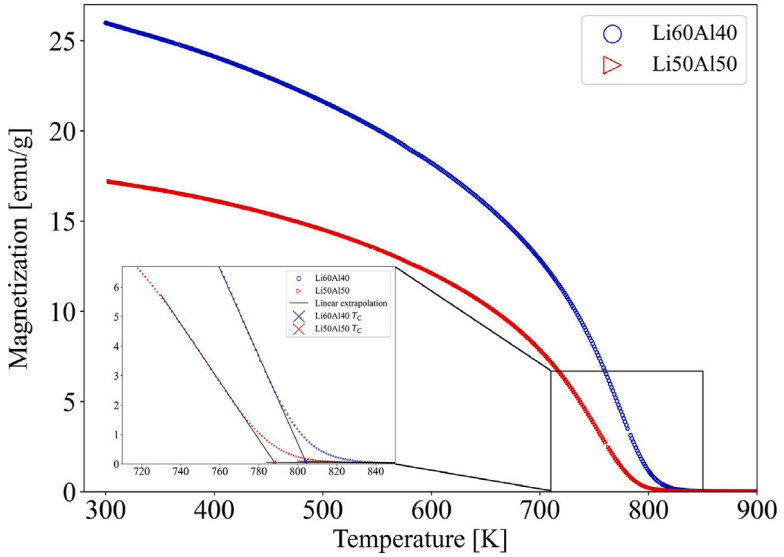

Fig. 8. T-dependent mass magnetization of Li60Al40 (blue circles) and that of Li50Al50 (red triangles). The evaluation of T_C at 804 K for Li60Al40 and 788 K for Li50Al50 are as shown in inset.

and the zero magnetic moments in both cubic magnetic subgroups are unlikely with Fe^{3+} ions with a strong spin moment having five unpaired electrons in the high spin state in the *3d* orbital, as resulting in a large discrepancy between the observed and the calculated HRNPD patterns (Supplementary Figure A.14a and A.14b). Note that a theoretical study of LFO confirmed the antiferromagnetic spin order between Fe1 and Fe2 only with large M_z components as the most stable spin arrangement in the cubic symmetry [23]. However, we want to emphasize that

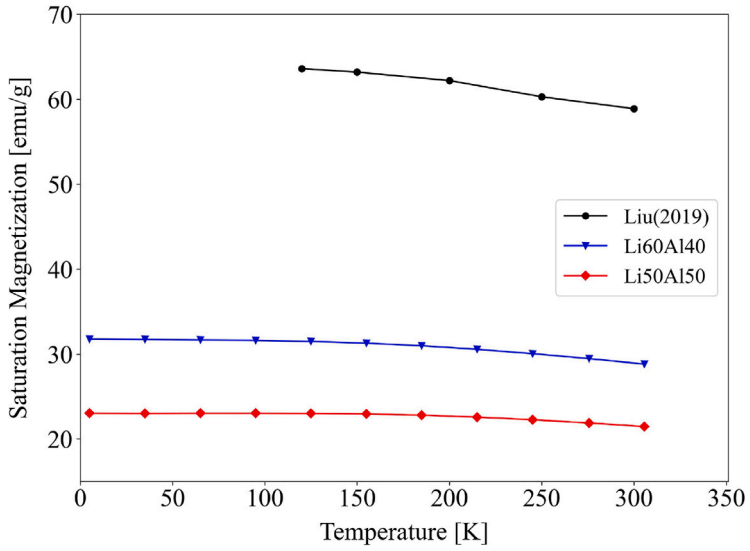

Fig. 9. Saturation magnetization of the compounds Li50Al50 (red squares) and Li60Al40 (blue triangles) at a DC magnetic field of 10 kOe. M_s values of LFO (black circles) are from [7].

Table 5
Structural formulae determined by Rietveld analyses using HRNPD data of Li60Al40 and Li50Al50, indicating octahedral [O] and tetrahedral [T] sites for Li^+, Al^{3+} and Fe^{3+}.

Lab code	Structural unit
Li60Al40	$(Li_{0.61(1)}Al_{0.39(1)})^{[O]}Fe^{[O]}[Fe_{0.805(4)}Li_{0.195(4)}]_2^{[O]}Fe_2^{[T]}O_8$
Li50Al50	$(Li_{0.48(4)}Al_{0.52(4)})^{[O]}Fe^{[O]}[Fe_{0.75(1)}Li_{0.25(1)}]_2^{[O]}Fe_2^{[T]}O_8$

this spin arrangement cannot be configured in the possible cubic MSGs (Supplementary Figure A.15), as mentioned above.

In fact, at all iron sites of Li60Al40 and Li50Al50 in the tetragonal MSG $\boldsymbol{P}4_32_1'2'$, the magnetic moment component in [001] (M_z) is dominant against the negligible small values of M_x and M_y with large errors as given in Supplementary Table A.11. Hence, with the constraints $M_x = M_y = 0$ at all Fe sites (Table 8), both Al-LFOs exhibit collinear ferromagnetic order in the B-sublattice at 300 K, based on HRNPD data. The magnetic moment modulus M at Fe1a (4.7(1) μ_B) in Li50Al50 is smaller than that in Li60Al40 (5.2(1) μ_B) without showing experimentally distinguishable OCC parameters equal to full occupation of Fe^{3+}. Besides, this one could contain vacancies at Fe1, even hardly provable in HRNPD data analyses, as aforementioned. The decreasing magnetic moment at Fe1a may possibly be explained by a higher disorder of spin orientations in the more Fe-dilute compound Li50Al50. Such a spin reorientation-dependent magnetization has been observed in several spinel-type ferrites [24–26]. On the other hand, an obvious dilute effect of Fe^{3+} can be seen with the decreasing modulus value of magnetic moments at Fe1b (2.4(2) μ_B) in Li50Al50 in comparison to that (2.6(2) μ_B) in Li60Al40. Furthermore, the magnetic moments at Fe1b are much smaller than those at Fe1a commonly in both compounds (Fig. 6), as a consequence of the preferred occupation of the non-magnetic Li^+ at Fe1b (Table 4).

The two magnetic sublattices are built with Fe^{3+} at the tetrahedral site Fe2 in the A-sublattice and those at the octahedral sites Fe1a and Fe1b in the B-sublattice, as shown in Fig. 7a and b, respectively. The A-sublattice exhibits a diamond lattice, where all magnetic spins of Fe^{3+} are parallel to each other in [00$\bar{1}$]. The B-sublattice forms a 2-dimensional kagome-like pyrochlore lattice of triangles of Fe^{3+}. The respective ferromagnetic arrangements in the A-sublattice of Li60Al40 and Li50Al50 are antiparallel to those of the respective B-sublattice (Fig. 7). The resulting ferrimagnetic compounds are realized by dominant antiferromagnetic interactions (J_{AB}) between the A- and the B-sublattice with different magnitudes of magnetic moments of Fe^{3+} (Fig. 6). Rietveld analyses with HRNPD data allowed the respective net magnetic moment magnitude per formula unit ($M/f.u.$) 2.6 and 1.9 μ_B for Li60Al40 and Li50Al50 ($M/f.u. = (1 \times |M_{Fe1a}| + 2 \times |M_{Fe1b}|) - 2 \times |M_{Fe2}|$). These $M/f.u.$ values indicate two different collinear magnetic arrangements at 300 K (Fig. 6), showing weak ferrimagnetism with the dilute-effect.

3.4. Magnetic properties

3.4.1. Curie temperatures and nearest-neighbor exchange interactions

It was expected that the dilute effect leads to lowering the thermal energy required for the ferri- to paramagnetic transition because J_{AB} is reduced by the replacement of Li^+ for the high magnetic Fe^{3+} in the B-sublattice [27]. Indeed, the Curie temperatures (T_C) 804 K for Li60Al40 and 788 K for Li50Al50 determined by temperature-dependent magnetization (Fig. 8) are much lower than T_C of LFO (890–950 K depending on microstructures [8,14,28]). In this way, in comparison to T_C of Li60Al40, the lower T_C of the Fe-dilute Li50Al50 can be understood (Fig. 8).

3.4.2. Saturation magnetization (M_s)

The T-dependent M_s [emu/g] curves of Li60Al40 and Li50Al50 commonly show marginal increases of M_s from 305 K down to 5 K (Fig. 9). Using Eq. (1), the $M/f.u.$ values 2.29 and 1.65 μ_B were calculated for Li60Al40 and Li50Al50, respectively, with the extrapolated values of M_s [$\mu_B/f.u.$] to 0 K (Supplementary Figure A.16):

$$M/f.u. = \frac{Mol.wt. \cdot M_s}{5585} \quad (1)$$

Another feature is a strong reduction of M_s in both Al-LFOs, compared to M_s of LFO [7]. This accords with the lower T_C values of Li60Al40 and Li50Al50 for the dilute effect with respect to LFO [29].

The weak ferromagnetism in Al-LFOs seems to be sensitive to competing (anti)ferromagnetic interactions by spin reorientation in the hyper-kagome B-sublattice (Fig. 7b), and probably by dynamics in intra- and inter-domains under external fields. In our preliminary AC magnetic susceptibility data acquisition with Li60Al40 at 1 Hz, the non-zero third harmonic term clearly indicated the presence of spin

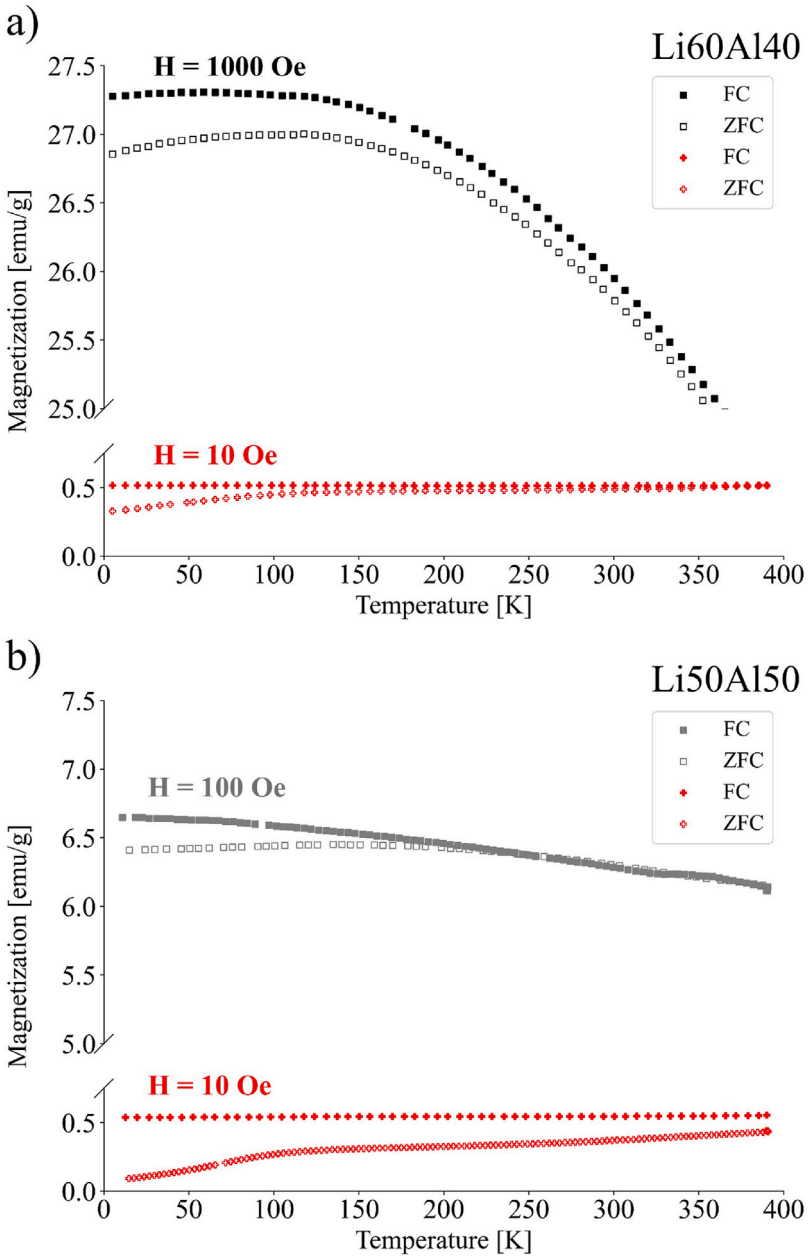

Fig. 10. T-H-dependent magnetization of Li60Al40 (a) and Li50Al50 (b).

Table 6
The lattice parameters **a** and **c** of variously Al-doped lithium ferrite compounds, with the lattice parameter changes (**Δa** and **Δc**) with respect to the lattice metric **a** of the pure lithium ferrite [7] at RT.

Lab code	**a** [Å]	**Δa** [Å]	**c** [Å]	**Δc** [Å]	|**a**-**c**| [Å]	Reference
LFO	8.3237					Liu et al. [7]
Li60Al40	8.2785(3)	−0.0452(3)	8.2630(5)	−0.0607(6)	0.0155(6)	This study
Li50Al50	8.2677(3)	−0.0560(4)	8.2506(6)	−0.0731(8)	0.0171(7)	This study

reorientation which is not associated to a change in spontaneous magnetization (Supplementary Figure A.17). Such spin-dynamic gives rise to spin-canting angles averaged out in diffraction techniques. However, we can confirm the dilute effect on M_s with the respective net magnetic moment per f.u. 2.6 and 1.9 μB for Li60Al40 and Li50Al50, resulting from the Rietveld analyses with HRNPD data collected in zero fields at 300 K. On the other hand, J_{AB} can complex vary with the substitutions of Li^+ for Fe^{3+} and Al^{3+} for Li^+ in the Al-LFO solid-solution compounds, as shown in Li-Zn spinel ferrite [30]. However, the average interatomic distances d(Fe1a-O-Fe2) and d(Fe1b-O-Fe2) in Li50Al50 do not concretely differ from those in Li60Al40 within their standard deviations (Supplementary Table A.9). Hence, a clear correlation of J_{AB} with those geometric parameters cannot be concluded in this study.

3.4.3. T-H-dependent ZFC and FC magnetization

ZFC and FC magnetization data of Li60Al40 acquired while applying the DC magnetic fields (H) 10 and 1000 Oe and those of Li50Al50 at 10 and 100 Oe in the temperature range 1.8–390 K are displayed in Fig. 10. The magnetization data of both Al-LFOs acquired while

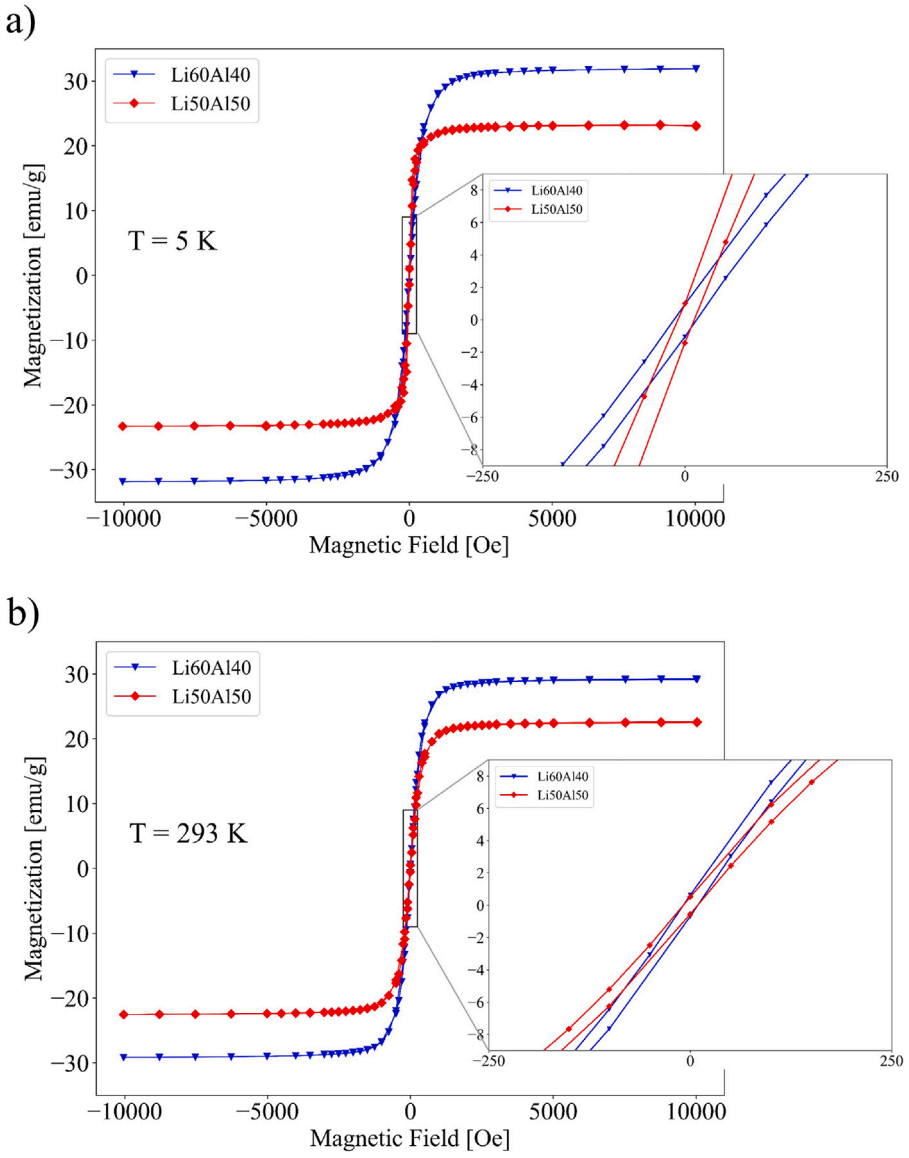

Fig. 11. Magnetization versus magnetic field at 5 K (a) and 293 K (b). The resulting hysteresis loops of both Li50Al50 (red squares) and Li60Al40 (blue triangles) indicate soft ferro-/ferrimagnetic behavior.

Table 7
Average polyhedral distortion degrees [%] in Li60Al40 and Li50Al50 based on the atomic structures refined with HRNPD data, compared to polyhedral distortions in LFO calculated with the structure model of Liu et al. [7]. Polyhedral distortion-induced dipole moments and their modulus values [eÅ] are scaled by the cation type and charge based on the refined OCC value at each site.

Lab code	Polyhedra	Site	Distortion [%]	Electric dipole moment [eÅ]			Modulus [eÅ]
				x	y	z	
LFO	LiO_6	Li1	0.1(1)	0	0	0	0
	FeO_6	Fe1	3.7(2)	0	−0.47(1)	0.47(1)	0.67(1)
	FeO_4	Fe2	1.1(1)	−0.08(1)	−0.08(1)	−0.08(1)	0.14(1)
Li60Al40	$(Li, Al)O_6$	Li1(Al1)	10.5(3)	0.97(17)	0.97(17)	0	1.38(17)
	FeO_6	Fe1a	1.1(1)	−0.33(1)	−0.33(1)	0	0.47(1)
	$(Fe, Li)O_6$	Fe1b	3.4(1)	0.12(1)	−0.51(1)	0.45(1)	0.69(1)
	FeO_4	Fe2	2.3(1)	0.04(1)	−0.03(1)	−0.01(1)	0.05(1)
Li50Al50	$(Li, Al)O_6$	Li1(Al1)	12.8(3)	1.19(5)	1.19(5)	0	1.68(5)
	FeO_6	Fe1a	1.2(1)	−0.29(1)	−0.29(1)	0	0.40(1)
	$(Fe, Li)O_6$	Fe1b	3.9(2)	0.01(1)	−0.32(1)	0.63(1)	0.71(1)
	FeO_4	Fe2	3.3(1)	0.13(1)	−0.14(1)	0.01(1)	0.19(1)

cooling at 10 Oe are nearly T-independent whereas the ZFC magnetization decreases continuously with decreasing temperature and then fast dropped from 100 K to 0.1 emu/g at the lowest measuring temperature 1.8 K. This branch point varies largely with the composition and the

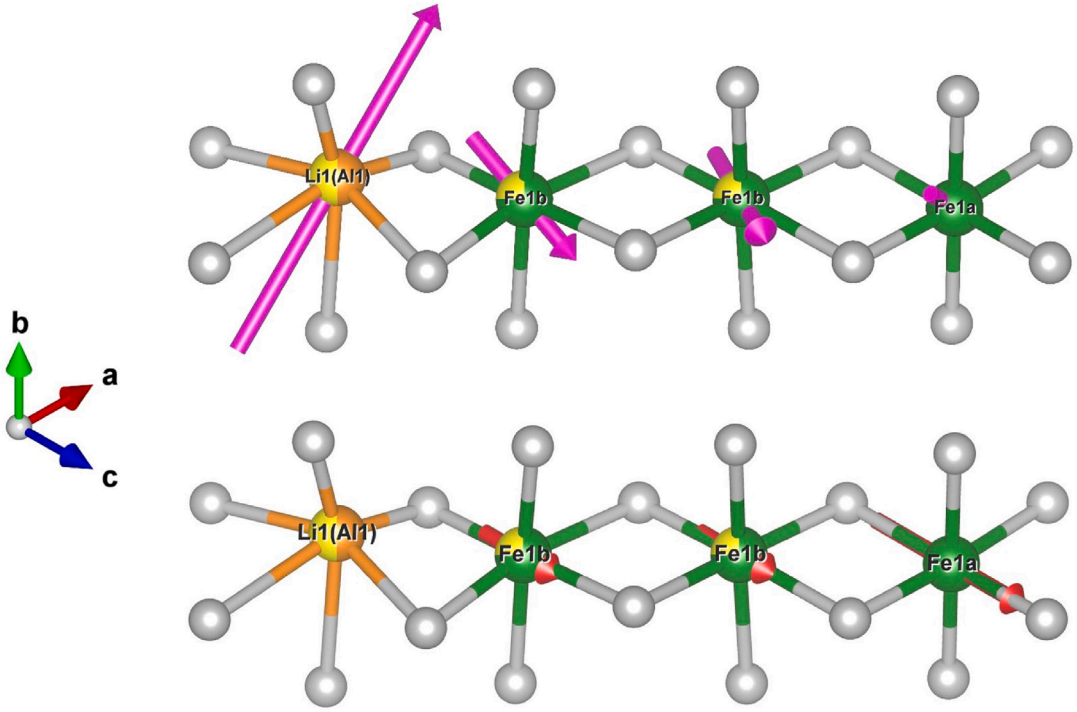

Fig. 12. Polyhedral distortion-induced electric polarization (pink arrows) and magnetic moments (red arrows) of Fe^{3+} in Li50Al50.

Table 8
Magnetic moment components M_x, M_y, M_z, and the modulus M [μ_B] at three independent Fe sites, resulted from Rietveld analyses with HRNPD data of Li60Al40 and Li50Al50 at 300 K for the correct tetragonal MSG $\boldsymbol{P}4_32_1'2'$. As shown in Supplementary Table A.11, all M_x and M_y refined with HRNPD data were extremely small with large errors, so that the constraints $M_x = M_y = 0$ were applied within the experimental uncertainty. The resulting magnetic moments per formula unit ($M/f.u.$) of these ferrimagnetic compounds are given in the last column.

Lab code	Site	M_x	M_y	M_z	M	M/f.u.
Li60Al40						2.6
	Fe1a	0	0	5.2(1)	5.2(1)	
	Fe1b	0	0	2.6(1)	2.6(2)	
	Fe2	0	0	−3.9(1)	3.9(1)	
Li50Al50						1.9
	Fe1a	0	0	4.7(1)	4.7(1)	
	Fe1b	0	0	2.4(1)	2.4(2)	
	Fe2	0	0	−3.8(1)	3.8(1)	

DC magnetic field: the ZFC and FC curve of Li60Al40 split at ~390 K and ~160 K with the respective H at 1000 and 10 Oe; in the case of Li50Al50, the FC-ZFC bifurcation is found at ~230 K and 400 K under 100 and 10 Oe, respectively. The difference at the lowest measured temperature between ZFC and FC is higher, with values of 0.238 emu/g at 100 Oe and 0.446 emu/g at 10 Oe. Such a bifurcation of FC-ZFC magnetization reminds of superparamagnetism, spin glass behavior, or domain dynamics [8]. These observations conclude an ease with spin-reorientation in Li50Al50 more than in Li60Al40 under a constant H.

3.4.4. Magnetization (M)-magnetic field (H) loops

LFO showed a nearly constant high coercivity (H_c) value of ~100 Oe in the temperature range of 120–300 K, [7] and a M_s of ~60 emu/g at 10 kOe at 300 K. In contrary, similarly small H_c values ~10 Oe were estimated in the M-H hysteresis loops of Li60Al40 and Li50Al50 at 293 K (Fig. 11b). At 5 K, the coercivity of both Al-LFOs increase insignificantly (Fig. 11a). Such a similar dilute effect on H_c and M_s has often been observed in spinel-ferrites [31].

The coercivity H_c represents magneto-crystalline anisotropy. Al-LFOs with extremely small H_c belong to soft magnetic materials to exhibit low magnetic anisotropy. The H_c values of Li60Al40 and Li50Al50 are indistinguishably similar H_c at a constant measuring temperature (Fig. 11 insets). However, based on the doping-percent (K) dependent coercivity $H_c = 0.96\,\mathrm{K}/M_s$ [27], H_c values and the anisotropy of Li50Al50 with the higher K and lower M_s might be higher than those of Li60Al40. But this was not resolved in their M-H loops. Hence, the static and dynamic disorder of Fe^{3+} spins in the B-sublattice particularly in Li50Al50 seem to be sensitive to external magnetic fields even below 2 kOe (Fig. 11). Therefore, an extended study of the interplay of polyhedral distortion-induced electric polarization in Al-LFOs (Fig. 12) under external electric, magnetic and mechanical fields at ambient conditions is of great interest.

4. Conclusion

The current study demonstrates that the partial substitutions of Al^{3+} only at the site for Li^+ and Li^+ for Fe^{3+} only at one of two Fe sites in the B-sublattice govern the symmetry lowering of atomic arrangements in the new Al-LFO solid solution compounds $(Li_{0.6}Al_{0.4})(Fe_{0.8}Li_{0.2})_2Fe_3O_8$ (Li60Al40) and $(Li_{0.5}Al_{0.5})(Fe_{0.75}Li_{0.25})_2Fe_3O_8$ (Li50Al50). The corresponding crystal-chemistry dictates the dilute effect in the resulting ferrimagnetic spin order in $\boldsymbol{P}4_32_1'2'$. The elucidation of the new ferrimagnetic structures using HRNPD data was critical and decisive to confirm their true atomic space group symmetry $\boldsymbol{P}4_32_12$.

The goal of this study was to enhance the polyhedral distortion in the LFO topology by chemical stress with Al^{3+} for Li^+. The polyhedral distortion accompanies with the magnetization of the title solid solution system. The first order of the bulk electric polarization might be zero in the point group 422, but the second- and high-order magnetoelectric coupling coefficients are predicted near RT. A drawback of Al-doped LFO compounds is that the polyhedral distortion-enhanced electric polarization is manipulated at the expense of dilute magnetization with respect to LFO.

As shown in several spinel-type compounds [2], the spin alignment in a triangle of magnetic cations in the B-sublattice is often imperfectly

antiparallel, leading to geometric fluctuation [32]. However, this is not for LFO-type compounds, as all magnetic spins in the B-sublattice are parallel to each other in [001] (Fig. 7b). However, a large geometric frustration would occur when strongly competing (anti)ferromagnetic interactions could be realized in the hyper-kagome lattice of Li50Al50 by various stimulation [2,26]. Further interesting issue is to study spin dynamics inter- and intra domains in the title solid-solution compounds. Their relative small tetragonality values could readily lead to form ferrodistortive and ferromagnetic domains with stressed domain boundaries. With this expectation, the title compounds deserved further structural and physical investigation under combined external fields.

CRediT authorship contribution statement

S. Inckemann: Writing – review & editing, Writing – original draft, Visualization, Investigation, Formal analysis. **S.-H. Park:** Writing – review & editing, Writing – original draft, Visualization, Validation, Supervision, Software, Resources, Project administration, Methodology, Investigation, Formal analysis, Data curation, Conceptualization. **A. Arauzo:** Writing – review & editing, Supervision, Methodology, Investigation, Formal analysis, Data curation. **M. Avdeev:** Writing – review & editing, Data curation.

Declaration of competing interest

The corresponding author SoHyun PARK discloses any potential competing or non-financial interests on behalf of all authors of this manuscript.

Acknowledgments

We thank Dr. A. Senyshyn at the neutron reactor FRM2 (Garching near Munich, Germany) for supporting HRNPD data collection.

Appendix A. Supplementary data

Supplementary material related to this article can be found online at https://doi.org/10.1016/j.jssc.2025.125325.

Data availability

Data will be made available on request.

References

[1] A. Sundaresan, N.V. Ter-Oganessian, Magnetoelectric and multiferroic properties of spinels, J. Appl. Phys. 129 (6) (2021) 060901, http://dx.doi.org/10.1063/5.0035825.

[2] H. Takagi, S. Niitaka, Highly frustrated magnetism in spinels, in: Introduction To Frustrated Magnetism: Materials, Experiments, Theory, Springer Berlin Heidelberg, Berlin, Heidelberg, 2011, pp. 155–175, http://dx.doi.org/10.1007/978-3-642-10589-0_7.

[3] Q. Zhang, W. Tian, R. Nepal, A. Huq, S. Nagler, J.F. DiTusa, R. Jin, Polyhedral distortions and unusual magnetic order in spinel $FeMn_2O_4$, Chem. Mater. 35 (6) (2023) 2330–2341, http://dx.doi.org/10.1021/acs.chemmater.2c03182.

[4] M. Schieber, High temperature phase transitions in lithium ferrite spinel single crystals, J. Inorg. Nucl. Chem. 26 (8) (1964) 1363–1367, http://dx.doi.org/10.1016/0022-1902(64)80115-9.

[5] A. Tomas, P. Laruelle, J.L. Dormann, M. Nogues, Affinement de la structure des formes ordonnée et désordonnée de l'octaoxopentaferrate de lithium, $LiFe_5O_8$, Acta Crystallogr. C 39 (12) (1983) 1615–1617, http://dx.doi.org/10.1107/S0108270183009488.

[6] J.M. Neto, P.H. Domingues, V.M.T.S. Barthem, F. de Souza Barros, M. Guillot, Magnetic properties of lithium ferrite doped with aluminum and gallium, J. Appl. Phys. 55 (6) (1984) 2338–2339, http://dx.doi.org/10.1063/1.333655.

[7] R. Liu, L. Pan, S. Peng, L. Qin, J. Bi, J. Wu, H. Wu, Z. Ye, The magnetoelectric effect in a cubic ferrimagnetic spinel $LiFe_5O_8$ with high coupling temperature, J. Mater. Chem. C 7 (2019) 1999–2004, http://dx.doi.org/10.1039/C8TC05615C.

[8] K.K. Kumawat, A. Jain, S.S. Meena, S.M. Yusuf, Structural and magnetic properties of ordered inverse spinel $Li_xFe_5O_8$, J. Alloys Compd. 856 (2021) 158849, http://dx.doi.org/10.1016/j.jallcom.2021.158849.

[9] A.I. Smolentsev, A.B. Meshalkin, N.V. Podberezskaya, A.B. Kaplun, Refinement of $LiFe_5O_8$ crystal structure, J. Struct. Chem. 49 (2008) 953–956, http://dx.doi.org/10.1007/s10947-008-0163-8.

[10] R. Saha, S. Ghara, E. Suard, D.H. Jang, K.H. Kim, N.V. Ter-Oganessian, A. Sundaresan, Magnetoelectric effect in simple collinear antiferromagnetic spinels, Phys. Rev. B 94 (2016) 014428, http://dx.doi.org/10.1103/PhysRevB.94.014428.

[11] S. Ghara, N.V. Ter-Oganessian, A. Sundaresan, Linear magnetoelectric effect as a signature of long-range collinear antiferromagnetic ordering in the frustrated spinel $CoAl_2O_4$, Phys. Rev. B 95 (2017) 094404, http://dx.doi.org/10.1103/PhysRevB.95.094404.

[12] Y. Sharma, R. Agarwal, L. Collins, Q. Zheng, A.V. Ievlev, R.P. Hermann, V.R. Cooper, S. KC, I.N. Ivanov, R.S. Katiyar, S.V. Kalinin, H.N. Lee, S. Hong, T.Z. Ward, Self-assembled room temperature multiferroic $BiFeO_3$-$LiFe_5O_8$ nanocomposites, Adv. Funct. Mater. 30 (3) (2020) 1906849, http://dx.doi.org/10.1002/adfm.201906849.

[13] C. Gao, C. Cao, J. Zhao, Structure and magnetic properties of epitaxial $LiFe_5O_8$ film with different growth temperatures, Appl. Phys. A 125 (566) (2019) http://dx.doi.org/10.1007/s00339-019-2850-z.

[14] V.J. Folen, Li ferrite, in: Magnetic and Other Properties of Oxides and Related Compounds, Springer Berlin Heidelberg, Berlin, Heidelberg, 1970, pp. 325–332, http://dx.doi.org/10.1007/10201438_101.

[15] V.P. Sakhnenko, N.V. Ter-Oganessian, The magnetoelectric effect due to local noncentrosymmetry, J. Phys.: Condens. Matter. 24 (2012) 266002, http://dx.doi.org/10.1088/0953-8984/24/26/266002.

[16] M.E. Fleet, The structure of magnetite, Acta Crystallogr. B 37 (1981) 917–920, http://dx.doi.org/10.1107/S0567740881004597.

[17] M. Avdeev, J.R. Hester, ECHIDNA: a decade of high-resolution neutron powder diffraction at OPAL, J. Appl. Crystallogr. 51 (6) (2018) 1597–1604, http://dx.doi.org/10.1107/S1600576718014048.

[18] K. Momma, F. Izumi, *VESTA*: a three-dimensional visualization system for electronic and structural analysis, J. Appl. Crystallogr. 41 (2008) 653–658, http://dx.doi.org/10.1107/S0021889808012016.

[19] Z. Song, Q. Liu, Effect of polyhedron deformation on 5d energy level of Ce^{3+} in lanthanide aluminum perovskites, Phys. Chem. Chem. Phys. 21 (2019) 2372–2377, http://dx.doi.org/10.1039/C8CP06052E.

[20] Z. Song, Z. Li, J. Zhang, Z. Chen, L. Suescun, Q. Liu, BFIP: an online tool to calculate the best fitted idealized polyhedron, J. Appl. Crystallogr. 56 (2023) 884–888, http://dx.doi.org/10.1107/S160057672300328X.

[21] P. Hirel, Atomsk: a tool for manipulating and converting atomic data files, Comput. Phys. Comm. 197 (2015) 212–219, http://dx.doi.org/10.1016/j.cpc.2015.07.012.

[22] R.D. Shannon, Revised effective ionic radii and systematic study of inter atomic distances in halides and chalcogenides, Acta Crystallogr. A 32 (1976) 751–767, http://dx.doi.org/10.1107/s0567739476001551.

[23] S.-Y. Kim, K.-S. Kim, U.-G. Jong, C.-J. Kang, S.-C. Ri, C.-J. Yu, First-principles study on structural, electronic, magnetic and thermodynamic properties of lithium ferrite $LiFe_5O_8$, RSC Adv. 12 (2022) 15973–15979, http://dx.doi.org/10.1039/D2RA01656G.

[24] M. Ajmal, A. Maqsood, Structural, electrical and magnetic properties of $Cu_{1-x}Zn_xFe_2O_4$ ferrites ($0 \le x \le 1$), J. Alloys Compd. 460 (1) (2008) 54–59, http://dx.doi.org/10.1016/j.jallcom.2007.06.019.

[25] H.M.I. Abdallah, T. Moyo, Superparamagnetic behavior of $Mn_xNi_{1-x}Fe_2O_4$ spinel nanoferrites, J. Magn. Magn. Mater. 361 (2014) 170–174, http://dx.doi.org/10.1016/j.jmmm.2014.02.077.

[26] J.M.D. Coey, Noncollinear spin structures, Can. J. Phys. 65 (10) (1987) 1210–1232, http://dx.doi.org/10.1139/p87-197.

[27] S.B. Narang, K. Pubby, Nickel Spinel Ferrites: a review, J. Magn. Magn. Mater. 519 (2021) 167163, http://dx.doi.org/10.1016/j.jmmm.2020.167163.

[28] E.N. Lysenko, V.A. Vlasov, A.V. Malyshev, E.A. Sheveleva, A.P. Surzhikov, Microstructure and electromagnetic properties of $LiFe_5O_8$ ferrite ceramics prepared from wet- and dry-milled powders, Ceram. Int. 47 (17) (2021) 23935–23941, http://dx.doi.org/10.1016/j.ceramint.2021.05.102.

[29] S. Mugiraneza, A.M. Hallas, Tutorial: a beginner's guide to interpreting magnetic susceptibility data with the curie-weiss law, Commun. Phys. 5 (2022) 2399–3650, http://dx.doi.org/10.1038/s42005-022-00853-y.

[30] S. Panchal, S. Raghuvanshi, K. Gehlot, F. Mazaleyrat, S.N. Kane, Cationic distribution assisted tuning of magnetic properties of $Li_{0.5-x/2}Zn_xFe_{2.5-x/2}O_4$, AIP Adv. 6 (5) (2016) 055930, http://dx.doi.org/10.1063/1.4944517.

[31] Y. Jiang, A. Sun, Microstructure and magnetic properties of Gd^{3+} doped Zn-Cu-Co nano ferrites, J. Mater. Sci.: Mater. Electron. 35 (2024) 1527, http://dx.doi.org/10.1007/s10854-024-13308-7.

[32] L. Balents, Spin liquids in frustrated magnets, Nature 464 (2010) 199–208, http://dx.doi.org/10.1038/nature08917.